arXiv:cond-mat/0510790v2 [cond-mat.supr-con] 5 Jun 2006

Theory for Inelastic Neutron Scattering in Orthorhombic High-T_c Superconductors

Andreas P. Schnyder[1], Dirk Manske[2], Christopher Mudry[1], and Manfred Sigrist[2]
[1] *Condensed Matter Theory Group, Paul Scherrer Institute, CH-5232 Villigen PSI, Switzerland*
[2] *Institut für Theoretische Physik, ETH Zürich, Hönggerberg, CH-8093 Zürich, Switzerland*
(Dated: February 2, 2008)

Using a Fermi-liquid-based theory we calculate the in-plane anisotropy of the spin susceptibility $\chi(\boldsymbol{q},\omega)$ for hole-doped high-T_c cuprates. Employing the two-dimensional one-band Hubbard model and a generalized RPA-type theory we consider anisotropic hopping matrix elements ($t_x \neq t_y$) and a mixing of d- and s-wave symmetry of the superconducting order parameter in order to describe orthorhombic superconductors. We compare our calculations with available inelastic neutron scattering data on untwinned $YBa_2Cu_3O_{6+x}$ and find good agreement. Furthermore, we predict a strongly anisotropic in-plane dispersion of the resonance peak.

I. INTRODUCTION

The spin dynamics plays an essential role in high-T_c cuprates. Superconductivity occurs very close to a Mott insulating state supporting a strong long-range antiferromagnetic (AF) order. Inelastic neutron scattering (INS) demonstrates, through the so-called commensurate and incommensurate peaks, the existence of magnetic collective phenomena in the superconducting state of hole-doped high-T_c cuprates intimately tied to superconductivity. [1, 2, 3, 4, 5, 6, 7]

Several theoretical scenarios have proposed a mechanism for superconductivity in the high-T_c cuprates attributed to magnetism. It has been argued that superconducting quasiparticles emerge from an exchange of AF spin fluctuations between Fermi-like quasiparticles [8, 9, 10] or from a recombination in momentum space of holons and spinons in a spin-charge-separated normal state.[11] In the stripe scenario, [12] strong electronic interactions result in normal and superconducting states in which spin and charge are separated in a predominantly one-dimensional region, called stripes, of the CuO_2 planes.

The incommensurate and commensurate peaks seen in INS on $La_{15/8}Ba_{1/8}CuO_4$ in Ref. 5 are interpreted in terms of excitation spectra in a bond centered stripe state with quasi or long-range magnetic order in the stripe picture of Refs. 13, 14, 15. Using a Fermi-liquid-like theory for itinerant quasiparticles, it was argued in Refs. 16, 17, 18, 19, 20, 21, 22, 23, 24, 25, 26 that the incommensurate and resonance INS peaks in $YBa_2Cu_3O_{6+x}$ (YBCO) or $Bi_2Sr_2CaCu_2O_{8+x}$ (Bi2212) are a fingerprint of a pure $d_{x^2-y^2}$-wave symmetry of the superconducting order parameter. In order to distinguish between the Fermi-liquid and stripe pictures applied to YBCO, a detailed analysis of the spin excitations in *untwinned* YBCO is helpful.

Pure $d_{x^2-y^2}$-pairing symmetry is only to be expected for underlying lattices with tetragonal symmetry. Most of the cuprates are known to show orthorhombic distortions. The high-T_c superconductor YBCO reveals a strong structural orthorhombic distortion as a function of doping. For example, a 60 $\%$ anisotropy in the London penetration depth between the a and b directions in the two-dimensional CuO_2 planes was found by Basov *et al.* [27] As YBCO is characterized by CuO-chains that are present only along the b direction and as these chains are believed to act as charge reservoirs that fill up with increasing doping x, a density functional calculation predicts a distorted Fermi surface (FS) in two dimensions. [28] This prediction of a two-dimensional anisotropic FS is consistent with angle-resolved photoemission spectroscopy (ARPES) studies by Lu *et al.* [29] who measured a strong a-b anisotropy in the electronic dispersion of monocrystalline $YBa_2Cu_3O_{6.993}$. In particular, they reported a 50 $\%$ difference in the magnitude of the superconducting gap in the vicinity of the $(\pi,0)$ and $(0,\pi)$ region of the first Brillouin zone (BZ), respectively. Smilde *et al.* [30] measured an a-b anisotropy of the Josephson current in junctions between monocrystalline $YBa_2Cu_3O_7$ and s-wave Nb, claiming that the obtained anisotropy can be well fitted by a 83% d-wave and 17% s-wave order parameter. Anisotropic responses are not limited to electromagnetic probes. The dynamical magnetic susceptibility measured by INS in monocrystalline and fully detwinned YBCO shows that the incommensurate peaks are strongly anisotropic in that their line shapes and intensities break the tetragonal symmetry. [31, 32, 33, 34] Thus, it has become necessary to go beyond a pure $d_{x^2-y^2}$ superconducting order parameter so as to incorporate the effects of crystalline hosts with orthorhombic symmetry.

Strongly anisotropic INS responses have both been interpreted as evidences for the proximity in parameter space to one-dimensional physics (stripe scenario) in Ref. 33 or to two-dimensional physics (Fermi-liquid-like scenario) in Ref. 34. The effects on INS of an orthorhombic dispersion of the superconducting quasiparticles were previoulsy studied in Refs. 35, 36, 37, 38. In this article, we analyze the observed anisotropy in INS within a conventional fermiology picture under the hypothesis that the observed anisotropies in the spin and charge response are caused by *both* a subdominant s-wave component in the superconducting gap and an orthorhombic BCS dispersion. To this end we use a phenomenological single-band tight-binding model describing BCS quasiparticles interacting weakly through a residual repulsive Hubbard interaction. The parameters entering the BCS dispersion are chosen so as to reproduce the measured values of the Fermi-surface and the BCS gaps at $(\pi,0)$ and $(0,\pi)$ close to optimally doped YBCO. The residual Hubbard interaction is fixed by the energy of the resonance at (π,π) at the same doping. [39]

The paper is organized as follows. Our model is described in Sec. II. Results for the dynamical magnetic susceptibility are presented in Sec. III. The qualitative behavior of the dy-

namical magnetic susceptibility is explained in Sec. IV. We summarize with Sec. V.

II. DEFINITION OF FERMIOLOGY

In this paper, we shall assume an effective one-band Hubbard Hamiltonian for each CuO_2 plane

$$\begin{aligned} H &= H_0 + H_1, && \text{(2.1a)} \\ H_0 &= -\sum_{\langle ij\rangle'\sigma} t_{ij} c^\dagger_{i\sigma} c_{j\sigma} - \mu \sum_{i\sigma} n_{i\sigma} \\ &\quad -\sum_{\langle ij\rangle} \left(\Delta_{ij} c^\dagger_{i\uparrow} c^\dagger_{j\downarrow} + \text{h. c.} \right), && \text{(2.1b)} \\ H_1 &= U \sum_i n_{i\uparrow} n_{i\downarrow}, && \text{(2.1c)} \end{aligned}$$

where the brackets $\langle ij\rangle$ and $\langle ij\rangle'$ denote the summation over the first nearest neighbors, and the first to fifth nearest-neighbors, respectively (see Fig. 1). Here, $c^\dagger_{i\sigma}$ is the creation operator of a quasiparticle with spin σ on site i, $n_{i\sigma} = c^\dagger_{i\sigma} c_{i\sigma}$ is the spin-dependent local number operator, t_{ij} is a hopping matrix element in the CuO_2 plane, μ is the chemical potential, Δ_{ij} is the superconducting gap, and U denotes a residual on-site (i.e., intraorbital) Coulomb repulsion. For simplicity we shall use a rigid-band approximation, by which all the effects of doping can be incorporated into a doping dependent chemical potential. The summation over the first few nearest-neighbors pairs of directed sites is most easily performed in the first BZ of the reciprocal space for the square lattice, in which case the noninteracting Hamiltonian is diagonal in reciprocal space

$$H_0 = -\sum_{\boldsymbol{k}\in \mathrm{BZ}} \left[\varepsilon_{\boldsymbol{k}} \sum_\sigma c^\dagger_{\boldsymbol{k}\sigma} c_{\boldsymbol{k}\sigma} + \Delta_{\boldsymbol{k}} \left(c^\dagger_{\boldsymbol{k}\uparrow} c^\dagger_{\boldsymbol{k}\downarrow} + \text{h.c.} \right) \right]. \tag{2.1d}$$

We shall choose the band parameters so as to fit qualitatively the FS as measured by ARPES. This can be done with the choice

$$\begin{aligned} \varepsilon_{\boldsymbol{k}} &= \frac{t_1}{2}(1+\delta_0)\cos k_x + \frac{t_1}{2}(1-\delta_0)\cos k_y \\ &\quad + t_2 \cos k_x \cos k_y \\ &\quad + \frac{t_3}{2}(1+\delta_0)\cos 2k_x + \frac{t_3}{2}(1-\delta_0)\cos 2k_y \\ &\quad + \frac{t_4}{2}\cos 2k_x \cos k_y + \frac{t_4}{2}\cos k_x \cos 2k_y \\ &\quad + t_5 \cos 2k_x \cos 2k_y + \mu. \end{aligned} \tag{2.1e}$$

The values for the hopping matrix elements are those that Norman used in Ref. 40 to fit photoemission experiments. The parameter $\delta_0 \neq 0$ breaks the tetragonal symmetry as the k_x and k_y directions in the BZ of the square lattice are not equivalent. In this paper we shall always choose a nonvanishing $\delta_0 < 0$ that corresponds to *effective hopping amplitudes larger along the k_y direction than along the k_x direction*. The superconducting gap is also chosen, on phenomenological grounds and out of simplicity, to be

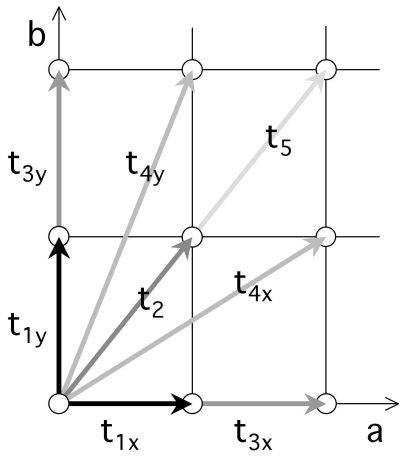

FIG. 1: The hopping parameters used in the tight-binding dispersion (2.1e) are $t_1 = -588.1$ meV, $t_2 = 146.1$ meV, $t_3 = 9.5$ meV, $t_4 = -129.8$ meV, and $t_5 = 6.9$ meV throughout this paper. An orthorhombic symmetry implies that rotation symmetry by $\pi/2$ is broken, i.e., that $t_{1x} \equiv t_1(1+\delta_0)/4$ is not equal to $t_{1y} \equiv t_1(1-\delta_0)/4$ and that $t_{3x} \equiv t_3(1+\delta_0)/4$ is not equal to $t_{3y} \equiv t_3(1-\delta_0)/4$.

$$\Delta_{\boldsymbol{k}} = \left(\Delta_x \cos k_x - \Delta_y \cos k_y \right)/2 + \Delta_s, \tag{2.1f}$$

where

$$0 < \Delta_s < \Delta_0 \equiv \left(\Delta_x + \Delta_y \right)/2. \tag{2.1g}$$

The condition $|\Delta_{(\pi,0)}| < |\Delta_{(0,\pi)}|$ that is observed in ARPES (see Ref. 29) can be implemented with the choice $\Delta_0 \equiv \Delta_x = \Delta_y$ and $\Delta_s > 0$ for the effective gap parameters. Of course, this choice is not unique, but since we are not concerned with deducing in a self-consistent manner the band and gap parameters from a microscopic model, we will make it for simplicity. In general, the effective energy scale U can encode an interaction that is strongly momentum dependent. For example in the $1/z$ expansion with z as the number of nearest neighbors, the repulsive channel of the interaction is peaked at the AF wave vector $\boldsymbol{Q}_{AF} = (\pi, \pi)$. [19, 20, 21, 41] This, however, will have no bearing on our conclusions and we choose U to represent a Hubbard on-site repulsion out of simplicity. The value for U throughout this paper is fixed by demanding that the position in energy of the resonance at the wave vector (π, π) coincides with the one observed in optimally doped YBCO.

The shape of the FS is depicted in Fig. 2(a) for the band parameters (see Ref. 40), $\mu = 110.0$ meV, $t_1 = -588.1$ meV, $t_2 = 146.1$ meV, $t_3 = 9.5$ meV, $t_4 = -129.8$ meV, and $t_5 = 6.9$ meV for $\delta_0 = 0$ (blue) and $\delta_0 = -0.03$ (red). The Fermi arcs of the orthorhombic FS are closer together in the $(0, \pm\pi)$ region than in the $(\pm\pi, 0)$ region of the BZ. This is a consequence of taking $\delta_0 < 0$. The opposite result follows from the choice $\delta_0 > 0$.[42] It is possible to use the chemical potential μ as a tuning parameter through a phase

transition of the Fermi surface topology. The FS in Fig. 2(a) is two-dimensional and holelike, i.e., it is closed around the four corners of the first BZ of the square lattice. Upon increasing the chemical potential to the value $\mu = 120$ meV, the FS [Fig. 2(a)] undergoes a transition to the quasi-one-dimensional topology [Fig. 2(b)] by which it is now open along the k_x direction but closed along the k_y direction in the first BZ of the square lattice. It has been argued in Refs. 20 and 43 that such a distorted FS can arise as a result of a $d_{x^2-y^2}$-wave Pomeranchuk instability due to strong electron-electron interactions. The absolute value of the superconducting gap $\Delta_{\boldsymbol{k}} = \Delta_0 \left(\cos k_x - \cos k_y\right)/2 + \Delta_s$ as a function of $\boldsymbol{k}$ with $\Delta_0 = 26$ meV and $\Delta_s = 3$ meV is shown in Fig. 2(c). The nodal points form two lines that are closed around the points $(\pm\pi, 0)$, respectively, in the extended BZ. The choice $\Delta_{\boldsymbol{k}} = \left(\Delta_x \cos k_x - \Delta_y \cos k_y\right)/2 + \Delta_s$ as a function of $\boldsymbol{k}$ with $\Delta_x = 20.8$ meV, $\Delta_y = 31.2$ meV, and $\Delta_s = 0$ (extended s-wave subdominant component) is shown in Fig. 2(d). A subdominant extended s-wave component with $\Delta_y > \Delta_x$ was found in Refs. 36, 44 after solving self-consistently a $t-t'-J$ model treated by the slave-boson approach.

In this paper we shall approximate the full frequency ω and momentum $\boldsymbol{q}$-dependent dynamical spin susceptibility $\chi(\omega, \boldsymbol{q})$ by the RPA approximation in terms of the noninteracting BCS-Lindhard response function $\chi_0(\omega, \boldsymbol{q})$. In turn, as the INS intensity in the superconducting state is proportional to the imaginary part $\chi''(\omega, \boldsymbol{q})$ of $\chi(\omega, \boldsymbol{q})$, we shall be computing

$$\chi''_{\rm RPA}(\omega, \boldsymbol{q}) = \frac{\chi''_0(\omega, \boldsymbol{q})}{\left[1 - U\chi'_0(\omega, \boldsymbol{q})\right]^2 + U^2 \chi''^2_0(\omega, \boldsymbol{q})}. \qquad (2.2)$$

A dispersing branch of incommensurate or commensurate peaks occurs whenever it is possible to find a frequency-momentum pair $(\omega^*, \boldsymbol{q}^*)$ that satisfies the dynamical Stoner criterion

$$1 - U\chi'_0(\omega^*, \boldsymbol{q}^*) = 0. \qquad (2.3)$$

The height of the peaks in a momentum or energy scan is determined by the size of $\chi''_0(\omega^*, \boldsymbol{q}^*)$ is. We define the resonance energy ω_{res} as ω^* at the AF wave vector $\boldsymbol{q}^* = (\pi, \pi)$. It is of order 43 meV for the band parameters of Fig. 1, the arithmetic average gap maximum Δ_0 taking the value of 26 meV, and the choice $U = 155$ meV.

III. NUMERICAL RESULTS FOR THE DYNAMICAL MAGNETIC SUSCEPTIBILITY

We have computed numerically the imaginary part of the RPA spin susceptibility (2.2) at a fixed transfer energy as a function of $\boldsymbol{q}$ for values of the transfer energy ranging from well below to well above the resonance energy $\sim$ 43 meV. The band parameters in Fig. 1 and the arithmetic average gap maximum $\Delta_0 = 26$ meV are fixed throughout this section. The values taken by the subdominant s-wave component Δ_s and the orthorhombic parameters δ_0 and $|\Delta_x - \Delta_y|$ are varied.

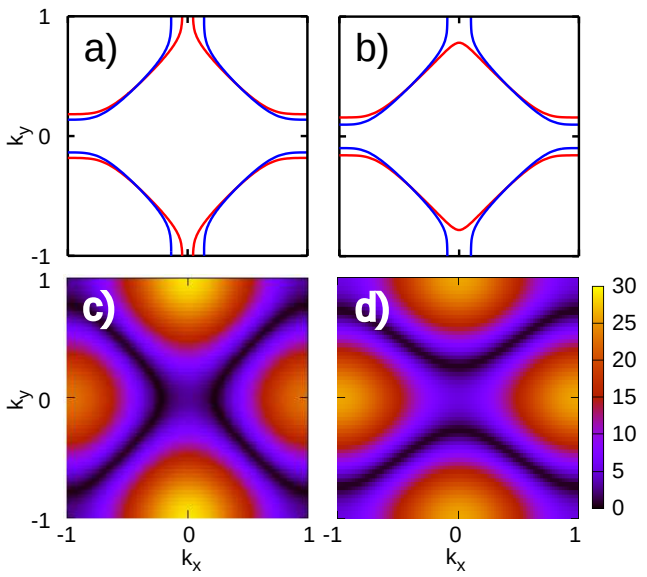

FIG. 2: (Color online) Panels (a) and (b) display the FS for the tight-binding dispersion (2.1e) with an orthorhombic distortion $\delta_0 = 0$ (blue) and $\delta_0 = -0.03$ (red) using two different values of the chemical potential $\mu = 110$ and $\mu = 120$ meV, respectively. The numerical values taken by the 5 hopping parameters $t_1, \ldots, t_5$ are given in Fig. 1. Panel (c) displays the absolute value of the superconducting gap $\Delta_{\boldsymbol{k}} = \Delta_0 \left(\cos k_x - \cos k_y\right)/2 + \Delta_s$ in meV using $\Delta_0 = 26$ meV and $\Delta_s = 3$ meV. Panel (d) displays the absolute value of the superconducting gap $\Delta_{\boldsymbol{k}} = \left(\Delta_x \cos k_x - \Delta_y \cos k_y\right)/2$ with $\Delta_x = 20.8$ meV and $\Delta_y = 31.2$ meV.

(i) *FS with orthorhombic anisotropy. Gap with isotropic s-wave subdominant component.* The case of a weakly orthorhombic distorted FS and of an orthorhombic gap induced by a weak s-wave subdominant component is displayed in Fig. 3. The band structure corresponds to that in Fig. 2(a) with $\delta_0 = -0.03$ and the anisotropic gap of Fig. 2(c), i.e., $|\Delta_x - \Delta_y| = 0$ while $\Delta_s = 3$ meV. Most of the intensity in $\chi''_{\rm RPA}(\omega, \boldsymbol{q})$ is concentrated on the perimeter of a diamond that is centered around the AF wave vector (π, π) for energies smaller than 40 meV. The area enclosed by this diamond decreases with increasing transfer energies. Remarkably, the maximum intensity is on the upper and lower corners of the diamond [intersection between the diamond and the vertical line passing through (π, π)] at the transfer energy of 20 meV whereas it has moved to the left and right corners of the diamond [intersection between the diamond and the horizontal line passing through (π, π)] at the transfer energy of 30 meV. The ratio of intensities at the upper and left corners of the diamond is of order 2 (1/2) for the transfer energy of 20 meV (35 meV). This anisotropy is much stronger than the orthorhombic anisotropy in the dispersion of the BCS quasiparticles (a 10% effect induces a 100% effect). For comparison, one finds that most of the intensity in $\chi''_{\rm RPA}(\omega, \boldsymbol{q})$ is to be found in a ring centered around (π, π) with four pronounced peaks at $(\pi \pm q_0, \pi)$ and $(\pi, \pi \pm q_0)$ in the tetragonal case, $\delta_0 = \Delta_s = 0$ [not shown here, see Fig. 4(a) in Ref. 37]. For energies larger than 40 meV the intensity in $\chi''_{\rm RPA}(\omega, \boldsymbol{q})$ is suppressed along the x

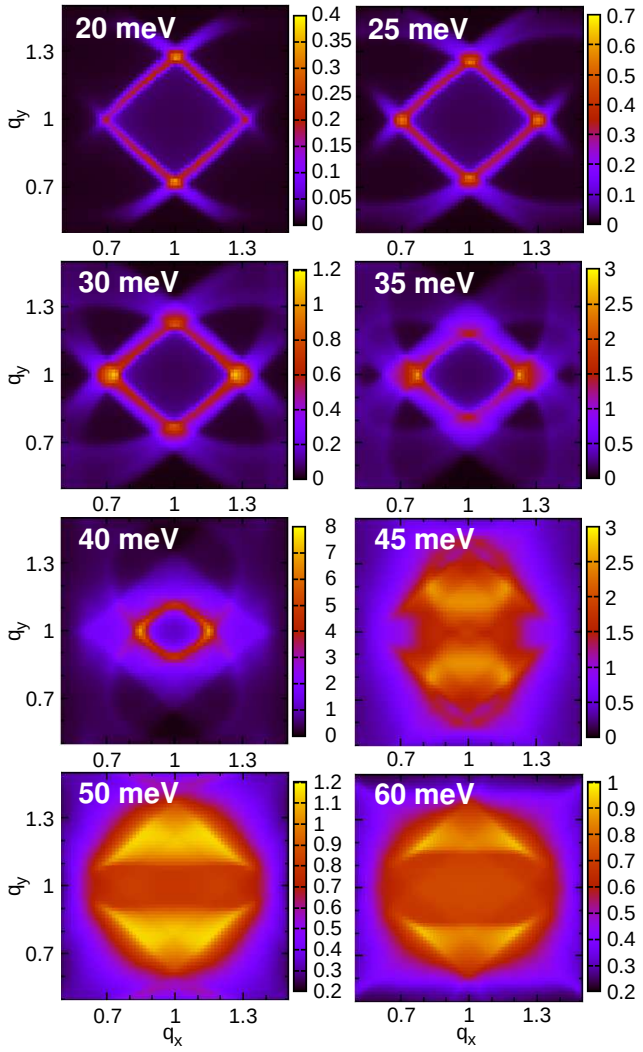

FIG. 3: (Color online) Imaginary part of the RPA spin susceptibility $\chi''_{\rm RPA}(\omega, \boldsymbol{q})$ for a constant transfer energy $\omega = 20\text{meV}, \ldots, 60\text{meV}$ as a function of $\boldsymbol{q}$ (in units of π) for the tight-binding band structure of Fig. 2(a) with $\delta_0 = -0.03$. We are also using $\Delta_0 = 26$ meV, $\Delta_s = 3$ meV, $U = 155$ meV, $T = 0$ K, and a damping $\Gamma = 1$ meV.

axis passing through (π, π) and is mostly concentrated in a disc that is centered around the AF wave vector.

(ii) *FS with orthorhombic anisotropy. Gap with tetragonal symmetry.* The case of a weakly orthorhombic distorted FS, $\delta_0 = -0.03$, and of a tetragonal gap, $|\Delta_x - \Delta_y| = \Delta_s = 0$, is displayed in Fig. 4(a). The only qualitative difference with Fig. 3 is the fact that the maximum intensity is always found at the left and right corners of a diamond centered at (π, π) below the resonance energy ~ 43 meV. Evidently, this difference at the lower end of the transfer energies ~ 20 meV can be ascribed to switching off the s-wave subdominant component to the gap. We thus conclude that, below the resonance energy, the anisotropy $t_y/t_x > 1$ favors dominant incommensurate peaks along the q_x direction while the subdominant s-wave component $\Delta_s > 0$ favors dominant incommensurate peaks along the q_y direction.

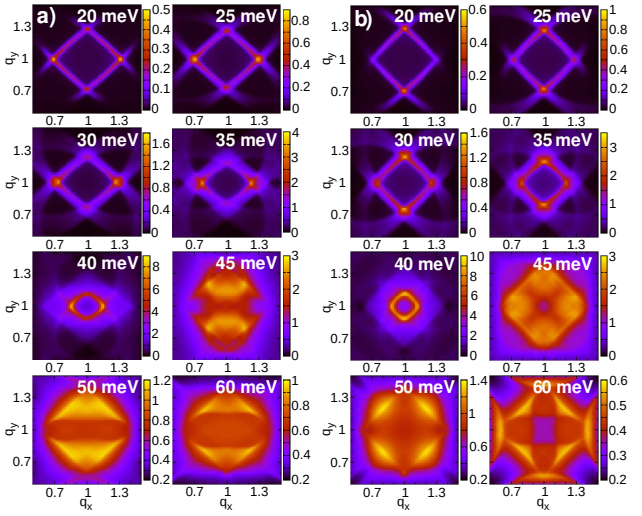

FIG. 4: (Color online) (a) Same as in Fig. 3 except for $\Delta_s = 0$. (b) Same as in Fig. 3 except for $\delta_0 = 0$.

(iii) *FS with tetragonal symmetry. Gap with isotropic s-wave subdominant component.* The case of a tetragonal FS, $\delta_0 = 0$, and of an orthorhombic gap induced by a weak s-wave subdominant component, $\Delta_s = 3$ meV, is displayed in Fig. 4(b). There are two qualitative differences with Fig. 3. The maximum intensity is always found at the upper and lower corners of a diamond centered at (π, π) below the resonance energy ~ 43 meV. The intensity distribution above ~ 43 meV is much less blurry than in Fig. 4(a) and displays some well defined arcs of dominant intensity centered about the diagonals passing through the center (π, π) of the magnetic BZ.

(iv) *FS with orthorhombic anisotropy. Gap with extended s-wave subdominant component.* The case of a weakly orthorhombic distorted FS, $\delta_0 = -0.03$, and of a gap with a strong orthorhombic distortion induced by $|\Delta_x - \Delta_y| = 10.4$ meV ($\Delta_y > \Delta_x$), but $\Delta_s = 0$, is displayed in Fig. 5(a). It is qualitatively very similar to Fig. 4(a). The maximum intensity is always found at the left and right corners of a diamond centered at (π, π) below the resonance energy ~ 43 meV. The anisotropy in the ratio between the intensities at the upper and left corners of the diamond are more pronounced than in Fig. 4(a). Since the anisotropy in the hopping parameters dominates over the anisotropy in the SC gap function, the opposite choice $\Delta_x > \Delta_y$ (not shown) leads to a qualitatively similar result, albeit with a reduced anisotropy ratio at low transfer energies ~ 20 meV.

At last we illustrate with Fig. 5(b) the fact that the distribution of intensities below the resonance energy ~ 43 meV in the RPA spin susceptibility tracks that in the bare Lindhard spin susceptibility. It is in this sense that the qualitative evolution of the intensity distribution in Fig. 3 between 20 and 35 meV is robust to changing the momentum dependence of the residual quasiparticle interaction in Eq. (2.1c).

IV. DISCUSSIONS

In this section we explain the qualitative behavior of the imaginary part of the RPA spin susceptibility $\chi''_{\rm RPA}(\omega,\boldsymbol{q})$ for an orthorhombic superconductor in terms of the properties of $\chi''_0(\omega,\boldsymbol{q})$ and the two-particle energy $E_2(\boldsymbol{q},\boldsymbol{k})$. We recall that in the limit of $T=0$ and for positive frequencies the imaginary part of the noninteracting BCS-Lindhard response function $\chi_0(\omega,\boldsymbol{q})$ simplifies to [25]

$$\chi''_0(\omega,\boldsymbol{q}) = \frac{\pi}{N}\sum_{\boldsymbol{k}} C^{+,-}_{\boldsymbol{q},\boldsymbol{k}}\,\delta\big(\omega - E_2(\boldsymbol{q},\boldsymbol{k})\big), \tag{4.1}$$

$$C^{+,-}_{\boldsymbol{q},\boldsymbol{k}} = \frac{1}{4}\left(1 - \frac{\varepsilon_{\boldsymbol{k}+\boldsymbol{q}}\varepsilon_{\boldsymbol{k}} + \Delta_{\boldsymbol{k}+\boldsymbol{q}}\Delta_{\boldsymbol{k}}}{E_{\boldsymbol{k}+\boldsymbol{q}}E_{\boldsymbol{k}}}\right), \tag{4.2}$$

$$E_2(\boldsymbol{q},\boldsymbol{k}) = E_{\boldsymbol{k}+\boldsymbol{q}} + E_{\boldsymbol{k}}, \tag{4.3}$$

where $E_{\boldsymbol{k}} = \sqrt{\varepsilon^2_{\boldsymbol{k}} + \Delta^2_{\boldsymbol{k}}}$ denotes the dispersion of the quasiparticles in the superconducting state. At a fixed wave vector $\boldsymbol{q}$ the imaginary part of the noninteracting spin susceptibility $\chi''_0(\omega,\boldsymbol{q})$ vanishes below the threshold frequency

$$\omega_c(\boldsymbol{q}) = \min_{\boldsymbol{k}\in \rm BZ} E_2(\boldsymbol{q},\boldsymbol{k}) \tag{4.4}$$

that defines the border to a continuum of particle-hole excitations. For a d-wave superconductor the low-energy border of the continuum has a nontrivial form (see Fig. 6). It is bounded by several segments of different curves along each of which $\chi''_0(\omega,\boldsymbol{q})$ exhibits either a jump (ω_1 and ω_2 in Fig. 6) or a kink (ω_d in Fig. 6) as a function of frequency, depending on whether the coherence factor $C^{+,-}_{\boldsymbol{q},\boldsymbol{k}}$ in Eq. (4.1) is vanishing for the wave vectors $\boldsymbol{k}$ contributing to $\chi''_0(\omega,\boldsymbol{q})$ at the border to the continuum. [21] The size of the jump in $\chi''_0(\omega,\boldsymbol{q})$ is controlled by two criteria: (i) How flat the two-particle dispersion at the corresponding minimum in $E_2(\boldsymbol{q},\boldsymbol{k})$ is, and (ii) by the degeneracy of the minimum itself. As explained in Ref. 25 the degeneracy of the minima $\min_{\boldsymbol{k}} E_2(\boldsymbol{q},\boldsymbol{k})$ is increased for $\boldsymbol{q}$ on a high symmetry axes of the magnetic BZ, i.e., on the k_x- or k_y-axes passing through (π,π) in the case of orthorhombic symmetry. The dispersion of the spin excitations in the presence of interactions is to a large extent determined by the behavior of $\chi''_0(\omega,\boldsymbol{q})$ at the border to the particle-hole continuum. A steplike discontinuity in the frequency dependence of $\chi''_0(\omega,\boldsymbol{q})$ results in a logarithmic singularity in $\chi'_0(\omega,\boldsymbol{q})$ due to the Kramers-Kronig relation. This in turn leads to a pole in $\chi''_{\rm RPA}(\omega,\boldsymbol{q})$ since the dynamical Stoner criterion (2.3) can be satisfied at a frequency $\omega^*(\boldsymbol{q}) < \omega_c(\boldsymbol{q})$. A finite damping Γ cuts off the logarithmic singularity in $\chi'_0(\omega,\boldsymbol{q})$, and the dynamical Stoner criterion can only be met for a sufficiently large size of the step in $\chi''_0(\omega,\boldsymbol{q})$ (see open diamonds in Fig. 6).

We find that an orthorhombic distortion in the band structure or in the superconducting order parameter partially lifts the degeneracy of the minima in $E_2(\boldsymbol{q},\boldsymbol{k})$ for $\boldsymbol{q}$ on the diagonal axes passing through (π,π). That is, for orthorhombic symmetry and $\boldsymbol{q}$ on the diagonal lines, there are four twofold degenerate critical frequencies $\omega_i(\boldsymbol{q})$ along which $\chi''_0(\omega,\boldsymbol{q})$ exhibits a jump. Whereas in the tetragonal case there are one fourfold and two twofold degenerate threshold frequency $\omega_i(\boldsymbol{q})$. Consequently, the intensity maxima in $\chi''_{\rm RPA}(\omega,\boldsymbol{q})$, for $\omega < \omega_{res}$ and for orthorhombic symmetry, lie on the horizontal and vertical axes passing through (π,π). This is in contrast to the tetragonal case, where the intensity maxima can occur on the diagonal axes as well.

In Fig. 6 we present the electron-hole continuum and the threshold frequencies $\omega_1(\boldsymbol{q})$, $\omega_2(\boldsymbol{q})$, and $\omega_d(\boldsymbol{q})$ for the directions (q_x,π) and (π,q_y) using the same parameters as in Fig. 3. Also shown is the continuation of the threshold

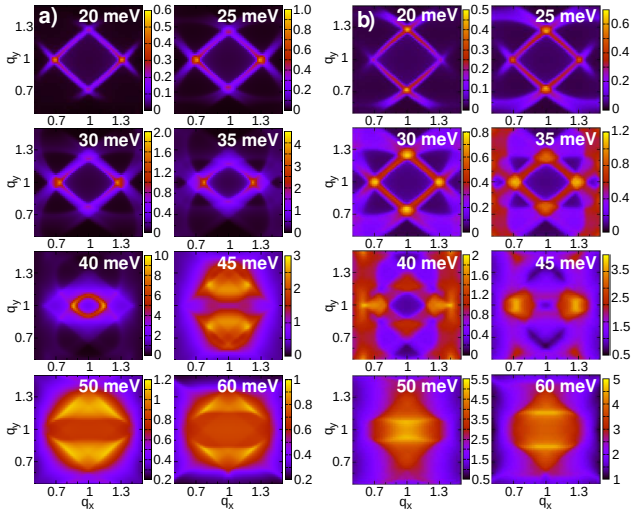

FIG. 5: (Color online) (a) Same as in Fig. 3 except for the gap $\Delta_{\boldsymbol{k}} = \left(\Delta_x \cos k_x - \Delta_y \cos k_y\right)/2$ with $\Delta_x = 20.8$ meV and $\Delta_y = 31.2$ meV from Fig. 2(d). (b) Imaginary part of the BCS-Lindhard spin susceptibility $\chi''_0(\omega,\boldsymbol{q})$ for a constant transfer energy $\omega = 20\text{meV},\ldots,60\text{meV}$ as a function of $\boldsymbol{q}$ (in units of π) for the same parameters as in Fig. 3.

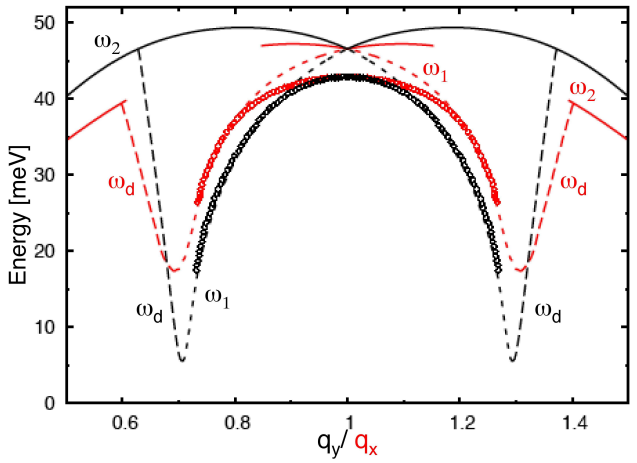

FIG. 6: (Color online) Momentum dependence of the threshold frequencies ω_1, ω_2, and ω_d calculated from $\min_{\boldsymbol{k}} E_2(\boldsymbol{q},\boldsymbol{k})$ using the same parameters as in Fig. 3. The threshold frequency as a function of (π,q_y) ((q_x,π)) is depicted in black (red). The open diamonds represent the position of the resonance peak.

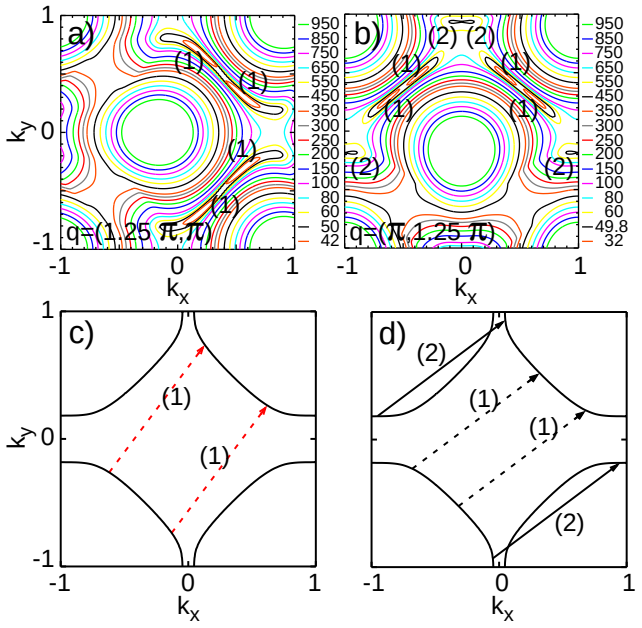

FIG. 7: (Color online) Panel (a) and (b) display the calculated $\boldsymbol{k}$-dependence of $E_2(\boldsymbol{q},\boldsymbol{k})$ in the first BZ for $\boldsymbol{q} = (1.25\pi,\pi)$ and $\boldsymbol{q} = (\pi,1.25\pi)$, respectively, using the same parameters as in Fig. 3. Panel (c) and (d) show the transitions between points on the Fermi surface yielding the threshold frequencies ω_1 and ω_2 for $\boldsymbol{q} = (1.25\pi,\pi)$ and $\boldsymbol{q} = (\pi,1.25\pi)$, respectively.

lines $\omega_2(\boldsymbol{q})$ into the continuum along which $\chi_0''(\omega,\boldsymbol{q})$ exhibits a second jump as a function of frequency. For tetragonal symmetry, similar results have been reported by Norman in Ref. 40. To illustrate the fact that the threshold frequencies correspond to (local) minima in the two-particle energy, we show in Fig. 7 the $\boldsymbol{k}$ dependence of $E_2(\boldsymbol{q},\boldsymbol{k})$ at the wave vectors $\boldsymbol{q} = (1.25\pi,\pi)$ and $\boldsymbol{q} = (\pi,1.25\pi)$ together with the associated scattering vetors between points on the FS [Fig. 7 (c) and Fig. 7 (d)]. In order to isolate the effect of an orthorhombic FS from the effect of a subdominant s-wave component we plot in Fig. 8 the dispersion of the threshold frequencies for $\Delta_s = 0$, $\delta_0 = -0.03$, and $\Delta_s = 3$ meV, $\delta_0 = 0$, respectively.

In the case of an orthorhombic FS and for $\boldsymbol{q}$ along the q_x direction the first scattering process [label (1) in Fig. 7] connects points that are further away from the gap *nodes* (see Fig. 2) than the corresponding points for $\boldsymbol{q}$ along the q_y direction. To the contrary, when $\boldsymbol{q}$ is on the horizontal axis passing through (π,π) the scattering vector of the second scattering process [label (2) in Fig. 7] connects points that are further away from the *antinodes* than the analogous points for $\boldsymbol{q}$ on the vertical axis.[45] This behavior reflects itself in the shape of the threshold lines [Figs. 8(a), 8(b), and 6]. It is found that $\omega_1(q,\pi) > \omega_1(\pi,q)$, whereas $\omega_2(q,\pi) < \omega_2(\pi,q)$ for any q. Since the local minima corresponding to the second scattering process are absent in the range $(0.65\pi \lesssim q_x \lesssim 0.85\pi, q_y = \pi)$ and $(1.15\pi \lesssim q_x \lesssim 1.35\pi, q_y = \pi)$ the line $\omega_2(\boldsymbol{q})$ along the q_x direction has a gap in this momentum range [Figs. 7(a) and 6]. As seen from Fig. 2(c) the inclusion of a subdominant s-wave component $\Delta_s = 3$ meV tilts the vector connecting the SC nodes from the diagonal line towards the x direction. Hence, the mismatch between the node-to-node vector and a wave vector $\boldsymbol{q}$ along the q_y direction is smaller than between the node-to-node vector and a wave vector $\boldsymbol{q}$ along the q_x direction [see Figs. 7(c) and 7(d)]. This leads to a smaller minimum of the particle-hole continuum along the q_y direction than along the q_x direction [Figs. 8(c), 8(d), and 6]. Finally, we note that the energy dispersion around the global mimina in $E_2(\boldsymbol{q},\boldsymbol{k})$ for $\boldsymbol{q}$ on the horizontal line is flatter than the dispersion for $\boldsymbol{q}$ on the vertical line (Fig. 7), which results in a larger jump in $\chi_0''(\omega,\boldsymbol{q})$ in the q_x direction than in the q_y direction.

As mentioned above the dispersion of the spin excitations tracks the behavior of the border to the particle-hole continuum $\omega_1(\boldsymbol{q})$. In Fig. 6 the position of the resonance peak are represented by open diamonds. We find that the downward parabola of the incommensurate peaks has a larger opening angle for $\boldsymbol{q}$ along the q_x direction than for $\boldsymbol{q}$ along the q_y direction. The dispersion is flatter in the q_x direction leading to incommensurate peaks that are broader in momentum space for a momentum transfer $\boldsymbol{q}$ on the horizontal axis than for $\boldsymbol{q}$ on the vertical axis. Moreover, if constant energy scans are taken, the incommensurate peaks along the q_x direction are about twice as intense than those along the q_y direction. This is due to the flatter energy dispersion of $E_2(\boldsymbol{q},\boldsymbol{k})$ for $\boldsymbol{q}$ on the x axis, and is in agreement with INS experiments recently performed by Hinkov *et al.* in $YBa_2Cu_3O_{6.85}$, i.e., near optimal doping (see Fig. 1 in Ref. 34). The fact that the magnetic response is larger along the q_x direction compared to the q_y direction for the energy range 30 meV $\leq \omega <$ 43 meV is robust as long as the anisotropy in the hopping parameters ($t_x < t_y$) dominates the anisotropy in the SC gap. For example, we have computed Fig. 3 with the band structure of Fig. 2(b), and found very similar results. The full parabolic dispersion of the resonance peak both along the q_x- and q_y direction still needs to be measured. For energies smaller than 25meV we find that the presence of a subdominant s-wave component in the SC gap shifts the intensity maxima in $\chi''_{\rm RPA}(\omega,\boldsymbol{q})$ at a constant transfer energy from the horizontal axis passing through (π,π) to the vertical axis.

V. SUMMARY

In summary, we have determined the effect of anisotropic hopping matrix elements and a mixing of d- and s-wave symmetry of the gap on the dynamical magnetic susceptibility of high-T_c cuprates within a Fermi-liquid-based theory. For transfer energies smaller than the resonance energy, ω_{res}, we find strongly anisotropic spin excitations on the horizontal and vertical axes of the magnetic BZ. The inclusion of anisotropic hopping parameters leads to a distortion of the square-like excitation pattern at a constant transfer energy to a rhombus shape. For $t_x < t_y$ and within the energy window $1/2\,\omega_{res} < \omega < \omega_{res}$ we have shown that the spin excitations along the q_x direction are about twice as intense than the ones

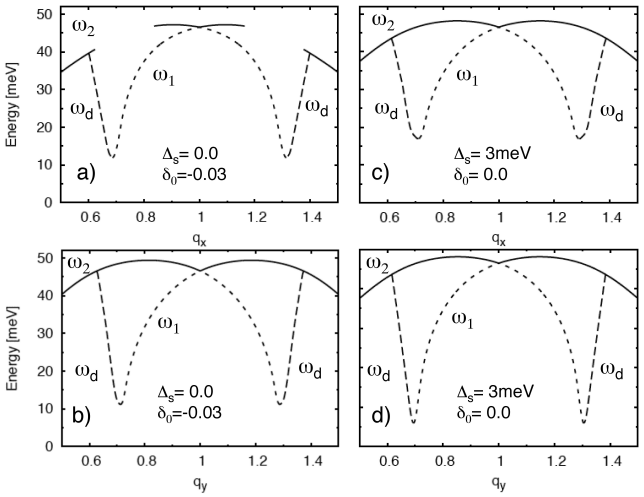

FIG. 8: Momentum dependence of the threshold frequencies ω_1, ω_2, and ω_d calculated from $\min_{\boldsymbol{k}} E_2(\boldsymbol{q},\boldsymbol{k})$ for different FS and gap parameters with $\boldsymbol{q} = (q_x, \pi)$ in panels (a) and (c) while $\boldsymbol{q} = (\pi, q_y)$ in panels (b) and (d). The FS parameters are those of Fig. 2(a) with $\delta_0 = -0.03$ while the gap is a pure d-wave gap with $\Delta_0 = 26$ meV and $\Delta_s = 0$ in both panels (a) and (b). The FS parameters are those of Fig. 2(a) with $\delta_0 = 0$ while the gap parameters are those of Fig. 2(c) with $\Delta_s = 3$ meV in both panels (c) and (d).

along the q_y direction. Furthermore, we predict considerable differences in the dispersion of the resonance peak along the (q_x, π)- and (π, q_y)-axes, respectively (see Fig. 6). The peaks along the q_x direction are both further apart and broader in momentum space compared to the peaks along the q_y direction.

The effect of a subdominant s-wave component in the superconducting gap is most prominent at small energies of about $\simeq 1/2\,\omega_{res}$. Assuming $\Delta_s > 0$, as demanded by ARPES measurements, [29] the subdominant s-wave component results in a rotation of the intensity maxima by 90^o relative to the excitation pattern at energies $1/2\,\omega_{res} \lesssim \omega < \omega_{res}$, and the spin gap becomes strongly anisotropic.

Between the resonance energy and a transfer energy of up to 50% larger than the resonance energy, the spin response remains anisotropic with a suppression of the intensity along the q_x direction. The anisotropy between the spin response along the inequivalent directions q_x and q_y decreases with an increasing transfer energy above the resonance energy. Intensities are negligible at transfer energies 400% larger than the resonance energy in sharp contrast to what is measured for $La_{15/8}Ba_{1/8}CuO_4$ in Ref. 5.

Acknowledgments

It is our pleasure to thank H. Yamase, S. Pailhes, V. Hinkov, B. Keimer, J. Mesot, and W. Metzner for useful discussions and H. Hilgenkamp for the prepublication copy of Ref. 30. This work was supported by the Swiss National Science Foundation under Grant No. 200021-101765/1 and the NCCR MaNEP. D. M. acknowledges financial support from the Alexander von Humboldt foundation.

[1] Ph. Bourges, L. P. Regnault, Y. Sidis, and C. Vettier, Phys. Rev. B **53**, 876 (1996).
[2] H. F. Fong, P. Bourges, Y. Sidis, L. P. Regnault, J. Bossy, A. Ivanov, D. L. Milius, I. A. Aksay, and B. Keimer, Phys. Rev. B **61**, 14773 (2000).
[3] P. Bourges, Y. Sidis, H. F. Fong, L. P. Regnault, J. Bossy, A. Ivanov, and B. Keimer, Science **288**, 1234 (2000).
[4] S. M. Hayden, H. A. Mook, P. C. Dai, T. G. Perring, and F. Dogan, Nature (London) **429**, 531 (2004).
[5] J. M. Tranquada, H. Woo, T. G. Perring, H. Goka, G. D. Gu, G. Xu, M. Fujita, and K. Yamada, Nature (London) **429**, 534 (2004).
[6] N. B. Christensen, D. F. McMorrow, H. M. Rønnow, B. Lake, S. M. Hayden, G. Aeppli, T. G. Perring, M. Mangkorntong, M. Nohara, and H. Tagaki, Phys. Rev. Lett. **93**, 147002 (2004).
[7] S. Pailhes, Y. Sidis, P. Bourges, V. Hinkov, A. Ivanov, C. Ulrich, L.P. Regnault, and B. Keimer, Phys. Rev. Lett. **93**, 167001 (2004).
[8] D. J. Scalapino, Phys. Rep. **250**, 329 (1995).
[9] A. Abanov, A. V. Chubukov, and J. Schmalian, Adv. Phys. **52**, 119 (2003).
[10] D. Manske, *Theory of Unconventional Superconductors* (Springer, Heidelberg, 2004).
[11] Patrick A. Lee, Naoto Nagaosa, and Xiao-Gang Wen, Rev. Mod. Phys. **78**, 17 (2006).
[12] S. A. Kivelson, I. P. Bindloss, E. Fradkin, V. Oganesyan, J. M. Tranquada, A. Kapitulnik, and C. Howald, Rev. Mod. Phys. **75**, 1201 (2003).
[13] M. Vojta and T. Ulbricht, Phys. Rev. Lett. **93**, 127002 (2004).
[14] G. S. Uhrig, K. P. Schmidt, and M. Grüninger, Phys. Rev. Lett. **93**, 267003 (2004).
[15] G. Seibold and J. Lorenzana, Phys. Rev. Lett. **94**, 107006 (2005).
[16] N. Bulut and D. J. Scalapino, Phys. Rev. B **53**, 5149 (1996).
[17] D. K. Morr and D. Pines, Phys. Rev. Lett. **81**, 1086 (1998).
[18] D. Manske, I. Eremin, and K. Bennemann, Phys. Rev. B **63**, 054517 (2001).
[19] J. Brinckmann and P. A. Lee, Phys. Rev. B **65**, 014502 (2002).
[20] H. Yamase and H. Kohno, J. Phys. Soc. Jpn. **70**, 2733 (2001); H. Yamase, J. Phys. Soc. Jpn. **71**, 1154 (2002); H. Yamase and H. Kohno, Phys. Rev. B **68**, 014502 (2003).
[21] F. Onufrieva and P. Pfeuty, Phys. Rev. B **65**, 054515 (2002).
[22] Ar. Abanov, A. V. Chubukov, M. Eschrig, M. R. Norman, and J. Schmalian, Phys. Rev. Lett. **89**, 177002 (2002).
[23] I. Sega, P. Prelovsek, and J. Bonca, Phys. Rev. B **68**, 054524 (2003).
[24] J.-X. Li and C.-D. Gong, Phys. Rev. B **66**, 014506 (2002).
[25] A. P. Schnyder, A. Bill, C. Mudry, R. Gilardi, H. M. Rønnow, and J. Mesot, Phys. Rev. B **70**, 214511 (2004).
[26] I. Eremin, D. K. Morr, A. V. Chubukov, K. H. Bennemann, and M. R. Norman, Phys. Rev. Lett. **94**, 147001 (2005).
[27] D. N. Basov, R. Liang, D. A. Bonn, W. N. Hardy, B. Dabrowski,

M. Quijada, D. B. Tanner, J. P. Rice, D. M. Ginsberg, and T. Timusk, Phys. Rev. Lett. **74**, 598 (1995).
[28] O. K. Andersen, A. I. Liechtenstein, O. Jepsen, and F. Paulsen, J. Phys. Chem. Solids **56**, 1573 (1995).
[29] D. H. Lu, D. L. Feng, N. P. Armitage, K. M. Shen, A. Damascelli, C. Kim, F. Ronning, Z.-X. Shen, D. A. Bonn, R. Liang, W. N. Hardy, A. I. Rykov, and S. Tajima, Phys. Rev. Lett. **86**, 4370 (2001).
[30] H. J. H. Smilde, A. A. Golubov, A. Ariando, G. Rijnders, J. M. Dekkers, S. Harkema, D. H. A. Blank, H. Rogalla, and H. Hilgenkamp, Phys. Rev. Lett. **95**, 257001 (2005); J. R. Kirtley, C. C. Tsuei, A. Ariando, C. J. M. Verwijs, S. Harkema, and H. Hilgenkamp, Natuer Physics **2**, 190 (2006).
[31] C. Stock, W. J. L. Buyers, R. Liang, D. Peets, Z. Tun, D. Bonn, W. N. Hardy, and R. J. Birgeneau, Phys. Rev. B **69**, 014502 (2004).
[32] C. Stock, W. J. L. Buyers, R. A. Cowley, P. S. Clegg, R. Coldea, C. D. Frost, R. Liang, D. Peets, D. Bonn, W. N. Hardy, and R. J. Birgeneau, Phys. Rev. B **71**, 024522 (2005).
[33] H. A. Mook, P. C. Dai, F. Dogan, and R. D. Hunt, Nature **404**, 729 (2000).
[34] V. Hinkov, S. Pailhes, P. Bourges, Y. Sidis, A. Ivanov, A. Kulakov, C. T. Lin, D. P. Chen, C. Bernhard, and B. Keimer, Nature **430**, 650 (2004).
[35] T. Zhou and J.-X. Li, Phys. Rev. B **69**, 224514 (2004).
[36] T. Zhou and J.-X. Li, Phys. Rev. B **72**, 134512 (2005).
[37] I. Eremin and D. Manske, Phys. Rev. Lett. **94**, 067006 (2005).
[38] E. Bascones and T. M. Rice, cond-mat/0511661 (unpublished).
[39] P. Dai, H. A. Mook, R. D. Hunt, and F. Dogan, Phys. Rev. B **63**, 054525 (2001).
[40] M. R. Norman, Phys. Rev. B **63**, 092509 (2001).
[41] Q. Si, J.-P. Lu, and K. Levin, Phys. Rev. B **45**, 4930 (1992).
[42] We would like to emphasize that our single-band model is a phenomenological one. It should be thought of as capturing the low energy physics of a more realistic microscopic model made of several bands describing, for example, the bilayer structure and the CuO chains in the YBCO family. Assuming orthorhombicity and the crystal structure of YBCO there are two competing phenomena. In an effective one-band Hubbard model it is natural to account for a lattice spacing along the b direction that is larger than along the a direction by hopping amplitudes $t_x > t_y$. However, the presence of the chain allows for a higher mobility for a charge carrier along the chain, which would lead to the opposite effect (cf. Ref. 35). What wins depends on microscopic details that are beyond our scope. Due to the much stronger anisotropy caused by the chains, one might naively expect that $t_y > t_x$, which is consistent with INS data.
[43] W. Metzner, D. Rohe, and S. Andergassen, Phys. Rev. Lett. **91**, 066402 (2003).
[44] H. Yamase (private communication).
[45] In Fig. 7(c) the scattering vector of type (2) is not shown, since the corresponding minima in $E_2(\boldsymbol{q}, \boldsymbol{k})$ do not exist.